Opto-Electronic Science

Review

September 2024, Vol. 3, No. 9

DOI: 10.29026/oes.2024.240005

Optical micro/nanofiber enabled tactile sensors and soft actuators: A review

Lei Zhang*, Yuqi Zhen and Limin Tong*

As a combination of fiber optics and nanotechnology, optical micro/nanofiber (MNF) is considered as an important multi-functional building block for fabricating various miniaturized photonic devices. With the rapid progress in flexible opto-electronics, MNF has been emerging as a promising candidate for assembling tactile sensors and soft actuators owing to its unique optical and mechanical properties. This review discusses the advances in MNF enabled tactile sensors and soft actuators, specifically, focusing on the latest research results over the past 5 years and the applications in health monitoring, human-machine interfaces, and robotics. Future prospects and challenges in developing flexible MNF devices are also presented.

Keywords: flexible opto-electronic devices; tactile sensors; soft actuators; optical micro/nanofibers

Zhang L, Zhen YQ, Tong LM. Optical micro/nanofiber enabled tactile sensors and soft actuators: A review. *Opto-Electron Sci* **3**, 240005 (2024).

Introduction

With the rapid development of personalized healthcare[1–3], virtual reality (VR) / augmented reality (AR)[4–6], and humanoid robots[7–9], optical tactile sensors have attracted intensive attentions due to their high sensitivity, high precision, fast response, and anti-electromagnetic interference[10–14]. Typically, an optical tactile sensor consists of a light source, a packaged sensing element, and a detector. By monitoring the change of output intensity, shift of resonant peak or interference spectra, a great number of high-performance tactile sensors have been demonstrated using silica optical fibers[15–18], polymer optical waveguides/fibers[19–22], hydrogel optical fibers[23–25], and optical micro/nanofibers (MNFs)[26–28]. Among them, MNFs possess excellent optical and mechanical properties, including strong evanescent field, low optical loss, wavelength scale diameter, small bending radius, various structures, and seamless connection with standard optical fiber[29–32]. The use of MNFs in tactile sensors can offer many exciting capabilities unavailable from other optical tactile sensors. For example, ultrahigh pressure sensitivity was achieved by using an optical nanofiber thanks to its prominent evanescent field and low stiffness[28]. MNFs can be mass-produced with controllable diameter, high transmission, high reproducibility, and very low cost by the fiber drawing technology[33–35]. Various flexible and stretchable MNF structures have been designed for measuring pressure, temperature, strain, bending, and so on. Furthermore, MNF tactile sensors show great potential for simultaneous detection of multi-parameters, integration with various substrates, and spatial multiplexing. Recent progresses in MNF tactile sensors have been well reflected by the numerous high-quality publications, especially in the applications of healthcare, human machine interface, and

State Key Laboratory of Extreme Photonics and Instrumentation, College of Optical Science and Engineering, Zhejiang University, Hangzhou 310027, China.

*Correspondence: L Zhang, E-mail: zhang_lei@zju.edu.cn; LM Tong, E-mail: phytong@zju.edu.cn

Received: 30 January 2024; Accepted: 22 April 2024; Published online: 26 July 2024

robotics.

On the other hand, MNFs have been used to assemble miniaturized photoactuators[36], which can produce a reversible mechanical deformation under light stimuli. In the recent years, photoactuators have attracted tremendous interest owing to their potential for soft robot and gripper application[37–39]. Most of photoactuators rely on free-space illumination, which requires a line-of-site low-loss optical path. While waveguide photoactuators can overcome this limitation[40–42], their actuating performances are fundamentally restricted by the nature of the standard optical fibers. For example, the relatively large size of the plastic optical fiber (e.g., 500 μm in diameter) results in a thick active layer, which may mitigate its bending angle[40]. Optical fiber taper, a kind of MNF with a tip diameter less than 1 micron, makes it possible to reduce the thickness of active layer and overcome the size mismatch between optical fiber and photo-responsive material. Moreover, the fiber taper provides a higher energy density than that of standard optical fiber due to the strong confinement of the MNF. Although the optical fiber enabled photoactuator is still in its infancy, the optical fiber taper offers an effective strategy to design high performance miniature photoactuators.

Several excellent review articles have been published on optical tactile sensors[43–46] and photoactuators[47,48], however, the role of MNFs has been underestimated. In this review, we focus on the recent advances in MNF enabled tactile sensors and actuators, and highlight the uniqueness of MNF for ultrasensitive and multifunctional sensors and miniaturized high-performance actuators. Figure 1 summarizes the on-going research in the four application areas. Our purpose is to introduce the key concepts and key papers for each topic. Firstly, we will discuss the fabrication and packaging of the MNF device. Secondly, we will summarize the sensing principle of the MNF enabled tactile sensors and their typical applications. Thirdly, we will discuss the MNF enabled photoactuators. Finally, we will give a brief summary and future prospect of MNF devices.

Fabrication and packaging of MNF for flexible tactile sensors

Since the demonstration of low-loss optical waveguiding in subwavelength-diameter nanofiber[49], flame-heated, laser-heated, and electrically heated taper drawing techniques have been widely used to fabricate MNFs[50]. In 2008, we fabricated a 680-nm-diameter nanofiber using

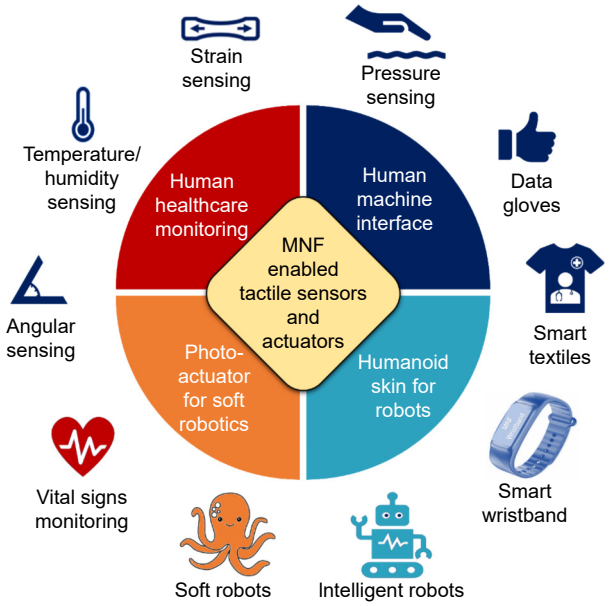

Fig. 1 | Characteristic properties and diverse functions and applications of recently developed tactile sensors and soft actuators.

an alcohol burner (Fig. 2(a-i)) for fast response humidity sensing[51]. Although this humidity sensor achieved fast response time and high sensitivity, the alcohol burner based taper drawing technique faced great challenge in large-scale manufacturing of uniform and low optical loss MNFs. In order to address this issue, the flame-heated taper drawing setup evolved from hand-held drawing, stage assisted drawing (Fig. 2(a-ii)) to automatic drawing (Fig. 2(a-iii)). Fang and Tong developed a series of methods[33–35] by real time monitoring optical transmission to precisely control the diameter of the MNF. Basically, there are several clearly observed abrupt drops of transmission intensity, and each drop indicates a cutoff of an optical mode, corresponding to a specific MNF diameter (Fig. 2(b-i)). Thus, by accurately measuring the time interval between two drops, one can precisely determine the time to stop taper drawing based on a target MNF diameter. Experimentally, the diameter accuracies can be 2 nm and 5 nm in the MNF diameter range of 360–680 nm[34], and 800–1300 nm[33], respectively. For a 10-cm-long, 1.05-μm-diameter MNF, the standard deviation over the whole MNF is 19 nm, yielding an excellent diameter uniformity as $\Delta d/L < 1.6\times10^{-7}$, where Δd is standard deviation over the whole MNF, and L is the length of the MNF[35]. Due to the smooth surface and uniform diameter (Fig. 2(b-ii)), the transmittance can be as high as 99.4% for a 10-cm-long MNF with a diameter of 1.2 μm. The low optical loss and high flexibility of

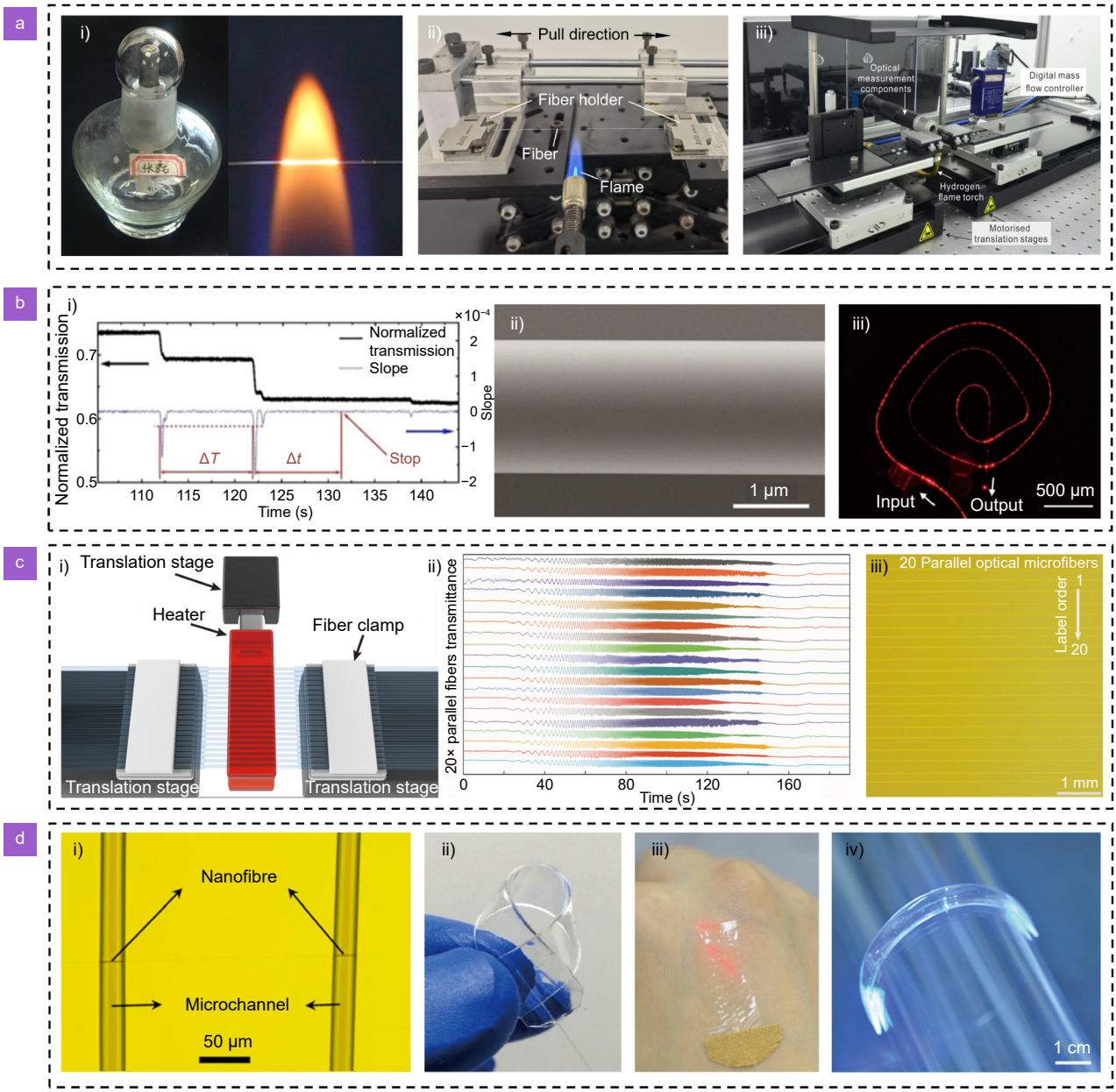

Fig. 2 | Fabrication and packaging the optical micro/nanofibers. (**a**) Evolution of flame-heated taper drawing setup. i) An alcohol burner and its flame; ii) A stage assisted taper drawing setup; iii) An automatic taper drawing setup. Figure reproduced with permission from ref.[28], under a Creative Commons Attribution 4.0 International License. (**b**) Fabrication of MNF with controlled diameter. i) Control of MNF diameter by real time measuring the time interval between two drops; ii) SEM image of an as-fabricated MNF with uniform diameter; iii) Spiral MNF guiding 633-nm-wavelength laser. Figures reproduced with permission from: i) ref.[33], © 2017 Optical Society of America; iii) ref.[28], under a Creative Commons Attribution 4.0 International License. (**c**) Fabrication of MNF array with an electric heater. i) Schematic of a taper drawing setup for fabricating MNF array; ii) Recorded the multimode-induced oscillation for 20 MNFs during the taper drawing process; iii) 20 MNFs in parallel. Figures reproduced with permission from: i-iii) ref.[52], under a Creative Commons Attribution 4.0 International License (**d**) Packaging the MNFs with PDMS. i) Micrograph of a microfluidic chip embedded MNF; ii) Bent PDMS packaged MNF in free space; iii-iv) PDMS packaged MNF attached on human skin (iii) and curved surface (iv), respectively. Figures reproduced with permission from: i) ref.[53], the Royal Society of Chemistry; ii-iii) ref.[28], under a Creative Commons Attribution 4.0 International License; iv) ref.[54], the Royal Society of Chemistry.

the MNF guarantee the MNF devices with a high transmittance (Fig. 2(b-iii)), which is very important for flexible sensors and photoactuators. Recently, Fang et al. proposed a parallel-fabrication approach (Fig. 2(c-i)) to simultaneously drawing multiple (up to 20) MNFs with almost identical geometries[52]. Alternatively, a home-made electric heater was used to generate a large hot zone with uniform temperature distribution. During the

taper drawing, the multimode-induced oscillation for each fiber starts almost simultaneously and is suppressed at approximately the same time (Fig. 2(c-ii)), indicating a nearly identical taper drawing environment. As a result, the as-fabricated MNF array shows high uniformity in terms of diameter and transmittance (Fig. 2(c-iii)). This parallel fabrication approach may open a door towards large scale fabrication of MNF devices.

In addition to large scale fabrication, a reliable package plays critical role in MNF devices, particularly in flexible MNF tactile sensors and actuators. Inspired by the PDMS microfluidic chip embedded MNF (Fig. 2(d-i))[53], almost all the reported MNF tactile sensors and actuators were packaged by PDMS, owing to its high transparency, high flexibility, low Young's modulus, low refractive index (~1.40), and excellent biocompatibility. Typically, a thin layer of PDMS film (e.g., 80 μm in thickness) can effectively isolate the evanescent fields, while maintaining high mechanical flexibility and low optical loss of the MNF. With the package of PDMS, an MNF tactile sensor can be bent in free space (Fig. 2(d-ii))[28], attached on human skin (Fig. 2(d-iii))[28] or curved surface (Fig. 2(d-iv))[54]. With reliable package, a sensitive MNF device shows high stability, robustness, and compact size, making it attractive for various applications with unique advantages.

Sensing mechanisms of MNF enabled tactile sensors

Since the basic model for microfiber sensors was proposed in 2005[55], a great number of physical, chemical or biological MNF sensors have been designed and fabricated based on evanescent-wave guiding properties of MNFs[56–58]. By measuring optical phase shift or changes in output intensity of the guided light, these MNF sensors offer excellent properties including high sensitivity, fast response, low power, and small footprint. MNF sensors based on intensity demodulation usually employ photodetectors to detect the light intensity changes caused by scattering, absorption, or re-emission of the guided light. Intensity demodulation has the advantages of simple system and good maneuverability, which has been widely used in chemical materials detection and biosensing. On the other hand, the intensity demodulation method directly detects the light intensity, the relative light intensity noise in the light component is relatively large, which may restrict its detection limit and resolution. Alternatively, the MNF sensors that adopt wavelength demodulation can be divided into resonators (e.g., whispering gallery mode (WGM) resonator[59–61], Fabry–Perot cavity[62,63], gratings (e.g., fiber Bragg grating[64–66], long period grating[67–69]), and interferometers (e.g., Mach-Zehnder interferometer)[70,71]. They measure external stimuli by detecting the wavelength shift, so the demodulation results are less affected by the light intensity noise. These wavelength demodulation MNF sensors have demonstrated high sensitivity, high resolution, and large dynamic range, however, the sensing system is more complex and expensive than that of intensity demodulation MNF sensors. Along with the rapid progress in wearable sensors[72], and increasing demands on flexible optical sensors, extensive research has been devoted to MNF-based optical flexible and wearable sensors, in which MNFs were employed as an artificial never sensing pressure, strain, bending angle, temperature, and relative humidity. Here we summarized the typical sensing mechanisms and the advantages and/or potentials of these miniaturized optical sensors categorized by MNF structures including biconical MNF, MNF ring resonator, MNF probe, MNF coupler, and microfiber Bragg grating (μFBG).

Biconical MNF

One of the most straightforward approaches to an MNF tactile sensor is using a biconical MNF, which has been successfully applied in physical[73,74] and chemical sensors[75,76]. Typically, a biconical MNF was embedded in a thin layer of flexible and stretchable low refractive index PDMS film[28]. The host of PDMS not only isolate the evanescent field of the MNF, but also transfer the exerted stimuli to the MNF with high fidelity (Fig. 3(a-i)). As shown in the inset of Fig. 3(a-i), the well confined symmetric mode of a straight MNF will evolve into an asymmetric profile with clear optical leakage when it is slight bent, making it a highly sensitive to micro deformation. Within the PDMS host film, the MNF can be straight-, U-, or wavy-shape (Fig. 3(a-ii)), offering additional flexibility for pressure, strain, or bending sensing. The engineerable MNF diameter and the tunable wavelength of the probing light offer an opportunity to achieve ultrahigh sensitivity or a wide detection range. For example, a suspended MNF tactile sensor (50-μm-thickness, 780-nm-diameter MNF) can feel the extreme low pressure down to 0.1 Pa with a high signal-to-noise ratio (Fig. 3(a-iii)) corresponds to a detection limit of about 7 mPa. Moreover, by taking advantage of PDMS's large negative

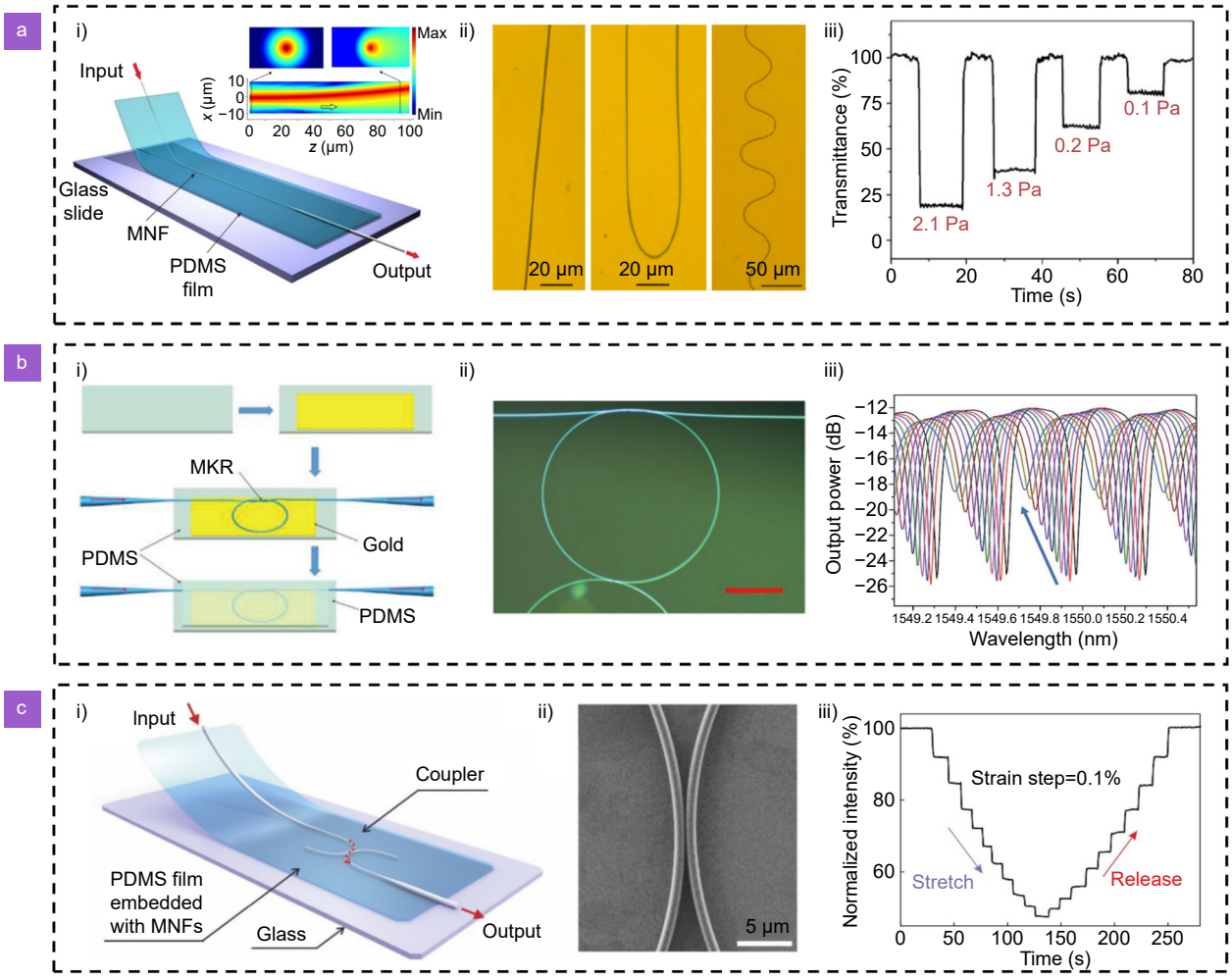

Fig. 3 | Sensing mechanisms of MNF enabled tactile sensors. (**a**) Biconical MNF enabled tactile sensor. i) Schematic of biconical MNF embedded in a thin layer of PDMS; Inset: Optical field intensity distributions of 900-nm-wavelength light guiding along a 1-μm-diameter glass MNF embedded in a 5°-bent MNF sensor; ii) Optical images of MNFs with different shapes; iii) Optical response of an MNF tactile sensor to weak pressure. Figures reproduced with permission from ref.[28], under a Creative Commons Attribution 4.0 International License. (**b**) MNF ring resonator enabled tactile sensor. i) Schematic of the fabrication process of the MNF ring resonator. ii) Microscope image of the MNF ring resonator on the gold film. Scale bar: 200 μm; iii) Resonant wavelength shift of the MNF sensor. Figures reproduced with permission from ref.[27], © 2018 WILEY-VCH Verlag GmbH & Co. KGaA, Weinheim. (**c**) MNF coupler enabled tactile sensor. i) Schematic of MNF coupler sensor; ii) SEM image of an MNF coupler; iii) Optical response of the coupler sensor in a stretch and release cycle. Figure reproduced with permission from ref.[93], under a Creative Commons Attribution 4.0 International License.

thermo-optic coefficient, temperature measurements, which plays a key role in tactile sensing, has been demonstrated for healthcare or robotics applications. In brief, the biconical MNF enabled tactile sensors pave the way toward a new category of optical tactile sensors due to its high sensing performance, controllable sensing structure (e.g., MNF diameter, bending radius, PDMS thickness), potential for large scale manufacturing, and simplicity in signal processing.

MNF resonator

Based on evanescent coupling at the overlapping area, an MNF can be assembled into a closed loop, knot, or coil, forming a high-quality whispering gallery mode (WGM) resonator[77,78]. Although a free-standing circular MNF resonator is easy to fabricate, it is mechanically fragile, and the MNF is susceptible to environmental disturbance. Enclosing a free-standing MNF resonator inside a low refractive index polymer is an effect approach to improve the robustness of an MNF resonator[79,80]. Benefitted from the high Q-factor and the miniaturized structure, the MNF resonators have been intensively investigated and applied for weak signal detection[81,82]. In 2018, Xu et al. proposed a hybrid plasmonic microfiber knot

resonator embedded in a PDMS membrane (Fig. 3(b-i, ii)) for healthcare monitoring[27]. By measuring the shift of the resonance peak (Fig. 3(b-iii)), the flexible and wearable MNF sensor achieved an ultrahigh gauge factor of 13700 and a pressure sensitivity of 0.83 kPa^{-1}. The WGM resonator provides a sensitive approach for designing wearable sensors for vital physiological monitoring applications. In addition to WGM resonator, MNF theta-shaped resonator[83], MNF Saganc resonator[84], multimode MNF inline interferometer[85] and MNF Mach-Zehnder interferometer[70] have been widely used for refractive index, force and ultrasonic sensing, providing more options for developing high performance flexible and wearable MNF sensing systems. However, its application in robotics or human-machine interface might be limited, because the MNF resonator sensing system often requires wavelength-swept laser and a high-resolution optical spectrum analyzer.

MNF probe

An MNF probe is a half biconical MNF, which is fabricated by nonadiabatic fiber tapering, followed by fiber cleaving. In order to increase the reflectivity of the MNF tip with a diameter of a few microns, a thin layer of gold can be coated on the enface of the MNF tip[86]. To work as a flexible tactile sensor, a low refractive index polymer package is necessary. Similar to the biconical MNF, the bending deformation of the MNF probe will lead to distortion of waveguide structure, resulting in modification of index profile in MNF probe[87]. When the effective refractive index of fundamental mode is lower than the cladding index, the fundamental mode will partly leak into the cladding and gradually transform into radiation modes, leading to the loss of light. For an MNF probe with a diameter of 2.1 μm, bending or pressure caused deformation can be obtained with a high sensitivity and flexibility by measuring the change of the reflected light. As a finger motion sensor, it achieved a bending angle sensitivity of −3.42%/(°) in the range of 5°–30° and −0.74%/(°) in the range of 30°–60°, respectively.

MNF coupler

MNF coupler provides an ultrasensitive sensing approach for weak strain or pressure detection, because the coupling efficiency is strongly dependent on the gap between the two MNFs and the coupling length[84,88,89]. Thus, any displacement between the two MNFs will be reflected upon the change of coupling efficiency. Note that, the change of ambient temperature may lead to a change of the coupling efficiency, because the MNF cladding usually possesses a giant negative thermal refraction coefficient (e.g., PDMS, -1.0×10^{-4} per °C)[90]. Fortunately, the impact of temperature on the weak strain sensing can be mitigated[91]. On the other hand, the temperature dependent coupling efficiency offers a promising approach to realize subtle change of ambient temperature[92]. Although the working range of this kind of sensors is limited, the ultrahigh sensitivity, fast response, and small footprint make them attractive for vital sign and micro-displacement monitoring. For example, Yu et al. proposed a flexible sensor with two evanescently coupled optical MNFs embedded in a PDMS film (Fig. 3(c-i))[93]. As shown in Fig. 3(c-ii), the gap between the two MNFs is only about 50 nm. The coupler sensor achieved a gauge factor of 64.5 and a strain resolution of 0.0012% which corresponds to elongation of 120 nm on a 1 cm long device (Fig. 3(c-iii)). Moreover, the fast temporal frequency response (up to 30 kHz) and high sensitivity (102 kPa^{-1}) bestowed the coupler sensor a capability for sound detection.

Microfiber Bragg grating

In addition to the abovementioned sensing mechanisms, the fiber Bragg grating represents the most successful sensing element with subwavelength or nano-engineered periodical structures in a single optical fiber[66,94,95]. The Bragg wavelength (λ_B) of the fiber Bragg grating is deduced from: $\lambda_B = 2n_{eff}\Lambda$, where Λ is the grating period and n_{eff} means the effective refractive index of the core mode. λ_B can respond to external parameters mediated by the variation of n_{eff} and Λ. When a FBG is bent, the interior of the structural unit is shortened by compression and the exterior of the structural unit is stretched by tensile forces. The length of the neutral line always remains constant between compression and extension. Therefore, the curvature of the neutral line can be used to represent the shape change of the fiber units. In general, there is a linear relationship between the bending curvature k and the Bragg wavelength drift $\Delta\lambda_B$. Thus, by simply measuring the Bragg wavelength drift of the FBG, one can obtain the curving degree. For example, Xu et. al developed a microfiber Bragg grating enabled wearable sensor for healthcare monitoring[96]. Due to the strain amplification effect of the microfiber, the sensor achieved enhanced sensitivity in pressure, bending angle and temperature.

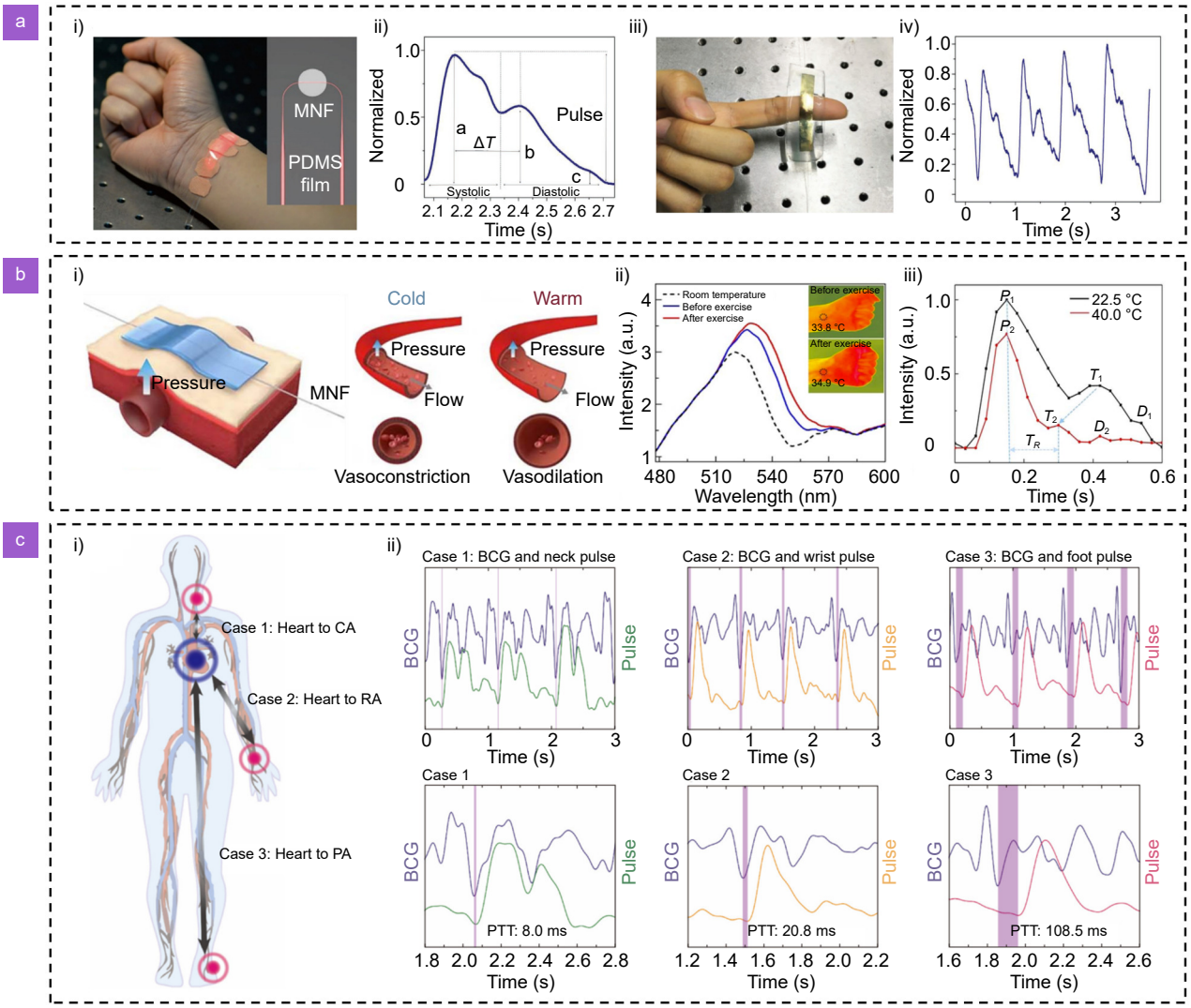

Fig. 4 | MNF tactile sensors for pulse monitoring. (**a**) Typical wrist pulse (i) and fingertip pulse (iii) sensors and corresponding waveforms (ii and iv). Figures reproduced with permission from: i) ref.[28], under a Creative Commons Attribution 4.0 International License; ii-iv) ref.[27], © 2018 WILEY-VCH Verlag GmbH & Co. KGaA, Weinheim. (**b**) Single MNF enabled wrist pulse sensor for simultaneous temperature and pulse measurement. i) Schematic of the pulse sensor; ii) Typical spectral response of the pulse sensor before and after exercise; iii) Comparison of the artery pulse pressure waveform variation with wrist temperature of 22.5 °C and 40.0 °C. Figures reproduced with permission from ref.[102], © 2022 Chinese Laser Press. (**c**) Spatiotemporal hemodynamic monitoring via configurable skin-like microfiber Bragg grating group. i) Schematic diagram of the measurement positions for the three cases; ii) The details of the BCG signal and pulse wave within one cardiac cycle. Case 1: simultaneous measurement of BCG and pulse wave at the carotid artery (CA). Case 2: simultaneous measurement of BCG and pulse wave at the radial artery (RA). Case 3: simultaneous measurement of BCG and pulse wave at the pedal artery (PA). Figures reproduced with permission from: ref.[104], under a Creative Commons Attribution 4.0 International License.

Application of MNF enabled tactile sensors

Healthcare monitoring

The pulse is a key biomedical signal containing various human physiological and pathological information highly related to cardiovascular diseases[97]. Typically, a flexible pressure sensor is attached onto the wrist (Fig. 4(a-i)) to detect the subtle vibration caused by the blood flow in radial artery. A typical pulse waves contains three peaks, named as percussion wave (P-wave), tidal wave (T-wave), and diastolic wave (D-wave) (Fig. 4(a-ii))[27]. The pulse waveform (e.g., the amplitude, time intervals between the peak are related to the systolic and diastolic blood pressure, the ventricular pressure, and the heart rate. For example, continuous and cuff-less blood pressure (BP) monitoring has been realized by combining the electrocardiogram and pulse transit time (PTT)[98]. However, a wrist pulse sensor often exhibits unstable signals

under hand motion because of the concave surface of the wrist[99]. By contrast, fingertips have a convex surface and therefore show great promises in stable and long-term pulse monitoring (Fig. 4(a-iii, iv))[27]. Nevertheless, the fingertip pulse signal is weaker than the wrist pulse, calling for highly sensitive sensors, such as MNF resonator sensor or MNF coupler sensor.

In order to develop a stable wrist pulse sensor, Li et al employed a flexible soft liquid sac to eliminate the misalignment and sensor position drift because the pressure change at any point in the incompressible static fluid caused by the pulse can be transmitted to upper PDMS film embedded with an MNF[100]. The high-fidelity pulse signal in the area of 20 × 20 mm^2 is successfully detected with uniform waveform.

On the other hand, the pulse waveforms are affected by body temperature, which may change the blood vessels vasodilation and vasoconstriction[101]. Therefore, it is necessary to measure temperature together with pulse monitoring to realize an accurate analysis of pulse waveforms. Yao et al. developed an MNF sensor that can detect both temperature and pressure by measuring the shift of a high-order mode cutoff wavelength in the short-wavelength range and the change of transmittance in the long-wavelength, respectively (Fig. 4(b-i))[102]. As shown in Fig. 4(b-ii), when the skin temperature increases 1.1 °C, the measured transmission peak presents a 1.3-nm wavelength shift. As a result, the pulse waveforms are quite different at cold (22.5 °C) and warm (40.0 °C) conditions in terms of the round-trip time (Fig. 4(b-iii)).

Despite of the success in real time wrist pulse monitoring[103], it is difficult to achieve systemic hemodynamic monitoring due to the lack of multichannel and time-synchronized the whole-body sensing system. Recently, Zhu et al. developed a continuous systemic hemodynamic measurement technique to monitor the whole-body blood circulation by using three flexible microfiber Bragg grating patches attached on neck, wrist, and foot, respectively (Fig. 4(c-i))[104]. By detecting the pulse wave at different superficial artery sites, the PTTs of three different cases (heart to carotid artery (CA), heart to radial artery (RA), and heart to pedal artery (PA)) can be detected and calculated. The waveforms and details of the synchronous ballistocardiogram (BCG) signal and pulse wave shows artery lengths and pulse wave propagation velocity dependent characteristics (Fig. 4(c-ii)). Relying on the multichannel and time-synchronized operation capability, the wearable MNF sensing system is capable of detecting the all-mechanical process of pulse wave propagation, making it a promising device for clinical medical diagnosis and daily health management.

In addition to pulse, respiration[91,105], body temperature[54,96,102], and body motion[54,87,106] sensing, the highly sensitive and miniaturized MNF have been used for ultrasound sensing and photoacoustic imaging. Combined with the coherent detection technology, Yang et al. proposed an ultrasound sensor by embedding a straight MNF into a thin layer of PDMS[107]. Ma et al. proposed an ultrasound sensor by sandwiching a microfiber loop between a pair of in-line Bragg gratings, forming a Fabry-Perot cavity that allows free delivery of ultrasound/ light beams and unique needle shaped ultrasound focusing along the penetration depth[108]. Benefiting from the large evanescent field characteristic of the microfiber, the proposed sensors realized highly sensitive ultrasound detection and demonstrated excellent performance in high-resolution photoacoustic imaging, which is a promising tool for noninvasive biomedical imaging and diseases diagnosis[109].

Human machine interface

We are already entering the era of the metaverse, in which virtual life and reality interact via various human machine interfaces[110,111], such as data glove[112,113], smart ring[114], wristband[115,116], socks[117], arm sleeve[118], clothes[119], and so on. Among them, data gloves have been intensively investigated due to their great potential for personalized healthcare, remote operation, motion capture, sign language recognition and VR space bidirectional communication. Compare to their electronic counterparts, MNFs enable data glove (Fig. 5(a-i)) offers unique properties including high bending angle resolution (Fig. 5(a-ii)), fast response, low power consumption, and immunity to electromagnetic interference[28]. The MNF enabled data gloves have been successfully used for controlling a virtual hand (Fig. 5(a-iii)) or a robotic hand (Fig. 5(a-iv)).

Although the data gloves can be light weight and desirable comfortability, there is an increasing requirement for imperceptible, convenient to use, and inexpensive human machine interface to facilitate natural and continuous interactions in the real physical world and online virtual ones. Inspired by the gesture-recognition wristband equipped electronic pressure sensors, Wang et al. reported an MNF pressure sensor enable wristband (Fig. 5(b-i))[120]. The key to the success of the optical wristband lies in three aspects: (1) the liquid sac can effectively

Fig. 5 | MNF tactile sensors for human machine interaction. (**a**) MNF bending sensor enabled data gloves. i) Image of an MNF glove with five bending sensors; ii) Bending-angle-dependent output of a typical MNF bending sensor; iii) Image of a virtual hand controlled by an MNF data glove; iv) Image of a robotic hand controlled by an MNF data glove. Figures reproduced with permission from ref.[28], under a Creative Commons Attribution 4.0 International License. (**b**) MNF pressure sensor enabled wristband. i) Schematic of the MNF enabled wristband; ii) Schematic of the MNF pressure sensor; iii) Cross-section of a wrist with a three-sensor wristband, indicating the position of the sensors and tendons; iv) Photograph of a three-sensor wristband; v) Application of the wristband for controlling a robotic hand based on hand gesture recognition. Figures reproduced with permission from ref.[120], under a Creative Commons Attribution License. (**c**) MNF pressure sensor enabled smart textiles. i) Schematic of optical MNF enabled smart textiles. ii) Optical image of the as-fabricated smart textiles. iii) Logic control of a robotic hand via the smart textile. iv) Machine learning enabled emotional human machine interface. Figures reproduced with permission from ref.[122], © 2022 Donghua University, Shanghai, China. (**d**) MNF humidity and pressure sensor enabled contact and proximity sensing. i) Schematic diagram of contact and proximity interaction; ii) Schematic of the contact and proximity sensor; iii) Responses of the sensor under finger approaching and contacting; iv) Photograph of the contact and proximity switch system for controlling the on/off of the LEDs. Figures reproduced with permission from ref.[125], © 2022 American Chemical Society.

mitigate the impact of sensor position on the detection of the movement of finger related tendons without sacrificing sensitivity (Fig. 5(b-ii)); (2) highly sensitive MNF pressure sensor on the skin can detect the subtle movement of tendon under the skin (Fig. 5(b-iii)); (3) The support-vector machine (SVM) machine-learning model

can effectively decode the signals from the MNF sensors. For a three-sensor wristband (Fig. 5(b-iv)), the maximum hand-gesture-recognition accuracy is about 94%, which is higher than that of electronic wristband using more sensors. To demonstrate its potential for human machine interaction, an MNF enabled wristband was used to remotely control a robotic hand (Fig. 5(b-v)).

In addition to the hand gesture recognition devices, significant efforts have been made to develop conductive textile to achieve lightweight, conformable, intuitive, and seamless interaction between human and machines[121]. Basically, the current strategies for manufacturing smart textiles are weaving functional fibers into textiles or depositing electric sensing materials on the fabric surface. However, sewability and washability represent two major challenges, which may hinder their practical applications. Ma et al. proposed an MNF enabled smart textile by integrating a PDMS patch embedded with MNF array with a piece of textiles (Fig. 5(c-i))[122]. The optical driven smart textile (Fig. 5(c-ii)) can be attached to cloth for working or detached from cloth during washing, offering an alternative manner to weaved-fibers based electronic HMIs. Benefiting from the warp and weft structure of the textile, the MNF enabled smart textile can feel slight finger touch or slip along the MNF, and classify the touch manners with the help of a SVM model. As proof-of-concept demonstrations, logic control of a robotic hand (Fig. 5(c-iii)) and communication with a virtual "xiaozhi" were realized (Fig. 5(c-iv)).

In addition to abovementioned pressure or bending sensor-based HMIs, humidity sensor provides a unique approach to realized proximity sensing[123,124], which is essential for human–machine interactions. Inspired by the somatosensory system of human skin, Liu et al. developed a hierarchically designed dual-mode interactive sensor (Fig. 5(d-i))[125] which consists of two designated MNFs, a Nafion–crystal violet (CV) layer, a stiff PDMS ring, and three PDMS packaging layers (Fig. 5(d-ii)). Thanks to the highly sensitive humidity and pressure sensing ability, together with a smart data processing unit, the integrated device achieved continuous detection of the full-contact events, including finger approaching, contacting, pressing, releasing, and leaving (Fig. 5(d-iii)). As a proof of concept, an HMI switch system shows collaborative on/off response to humidity and/or pressure change caused by the bare/gloved fingers (Fig. 5(d-iv)).

Robotic sensors

It is essential for a humanoid robot to equip a skin-like tactile sensor with multifunctional sensing ability to realize dexterous manipulation and tactile feedback[126,127]. The epidermis with high elastic modulus and the fingerprint patten plays critical roles in amplifying and transferring external stimuli to sensory receptors. By mimicking the structural characteristics of human finger skin, Jiang et al. designed and fabricated an MNF tactile sensor with fingerprint-like parallel ridges (Fig. 6(a-i))[128]. Benefiting from fingerprint structures, a robotic gripper installed with the MNF tactile sensor can detect and discriminate grasping force as well as contact slippage when performing object manipulation tasks (Fig. 6(a-ii)). Moreover, slipping related information can be derived by applying wavelet transform to the output signal (Fig. 6(a-iii)).

In addition to slip detection, a multitude of tactile sensors with a capability of measuring force, deformation, temperature, and hence allowing for the discrimination of hardness, texture, and thermal conductivity is now playing a vital role in humanoid robots. To this end, Tang et al. designed and fabricated a multimodal (force and thermosensitive) robotic skin by embedding MNF into PDMS films with special modules as shown in Fig. 6(b-i)[129]. The MNF tactile sensor can enable a commercial robot to emulate human behaviors, including adaptive grasping of a cup of coffee (Fig. 6(b-ii)) and recognition of object texture (Fig. 6(b-iii)).

Recently, robot assistants, which share working workspace with human users, are becoming a cutting-edge application of smart robots. To improve the safety and avoid collision, a robot should able to detect humans, be aware of risk, and make fast responses to minimize the risk of injury. Typically, the human body temperature is higher than the ambient temper, it is possible for a robot to detect humans by real time measuring the subtle temperature variation near the robot. To this end, Song et al. developed an ultrasensitive temperature sensor based on twisted MNFs (Fig. 6(c-i))[92]. Because the coupling efficiency between the twisted MNFs is highly sensitive to the refractive index of the PDMS cladding, which has a high thermo-optic coefficient, the sensor achieves a sensitivity of −30 nm/°C and a resolution of 0.0012 °C. As illustrated in Fig. 6(c-ii), the output intensity curve shows a distance dependent response to a human hand in a range of 0–15 cm. When a robotic arm equipped with the temperature sensor, it can effectively

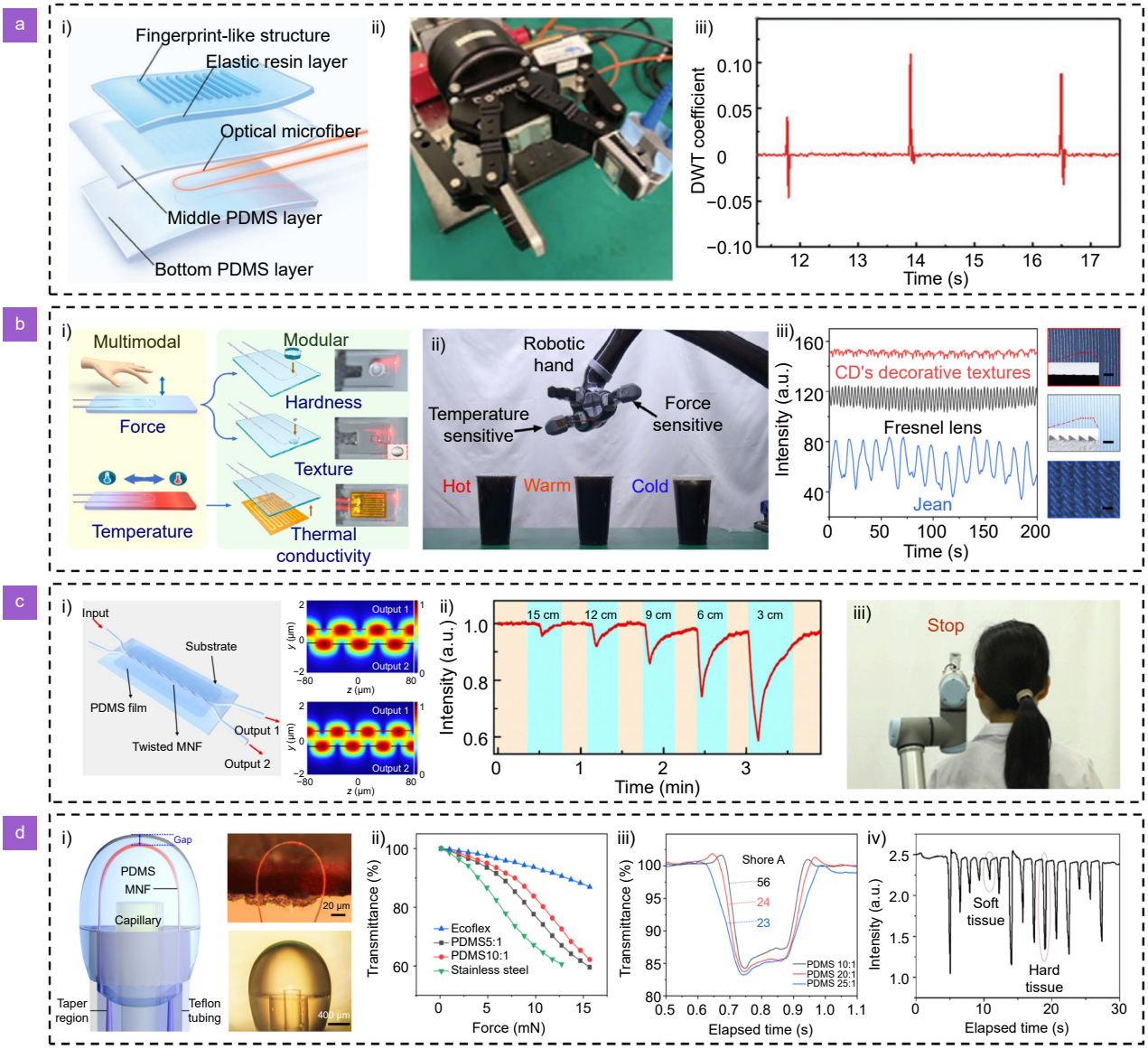

Fig. 6 | MNF tactile sensors for robots. (**a**) Finger-skin-inspired MNF sensor for force sensing and slip detection. i) Schematic of the finger-skin-inspired MNF sensor; ii) Photograph of a robotic gripper equipped with an MNF sensor; iii) Discrete wavelet transform of the response curves with three peaks. Each peak indicates a slip of the object grasped by the robotic hand. Figures reproduced with permission from ref.[128], © 2021 Wiley-VCH GmbH. (**b**) Multimodal and modular MNF sensors for multifunctional humanoid tactility. i) Schematic of the multimodal and modular MNF sensors; ii) A robotic hand equipped with the MNF sensor is ready to recognize and pick up a cup of warm coffee. iii) The responses of the MNF sensor for the texture recognition of CD, Fresnel lens and jean. Figures reproduced with permission from ref.[129], under a Creative Commons Attribution License. (**c**) Twisted MNFs enabled ultrasensitive temperature sensor. i) Schematic of the twisted MNFs sensor; ii) Response of hand proximity with different distances; iii) The robot with temperature feedback can effectively avoid undesired collisions. Figures reproduced with permission from ref.[92], © 2023 American Chemical Society. (**d**) MNF-enabled compact tactile sensor for hardness discrimination. i) Schematic and photograph of the U-shaped MNF-enabled compact tactile sensor; ii) Optical response of the sensor to objects with different hardness; iii) Intensity curves corresponding to objects with different hardness; iv) Intensity curves corresponding to pork liver and an adductor muscle. Figures reproduced with permission from ref.[130], © 2021 American Chemical Society.

detect the existence of a human, and trigger avoiding collision feedback (Fig. 6(c-iii)).

With the rapid development of minimally invasive surgery and surgy robots, there is an increasing demand for miniaturized tactile sensors than can provide tactile information during the surgery. To this end, Tang et al. developed an MNF enabled compact tactile sensor with a diameter of 1.5 mm (Fig. 6(d-i))[130]. The sensor can be operated in either scanning or tapping mode, achieving a hardness resolving ability even beyond the human hands.

For example, it can discriminate different materials by analyzing the slope of the response curve (Fig. 6(d-ii, iii)). As a proof-of-concept demonstration, the hardness discrimination of pork liver and an adductor muscle was experimentally realized (Fig. 6(d-iv)). Such MNF-enabled compact tactile sensors may pave the way for hardness sensing in tissue palpation, surgical robotics, and object identification.

MNF enabled photoactuators

Typically, photoactuators convert light energy into thermal (expansion/contraction, molecule adsorption/desorption, and phase transition) or chemical energy (photoisomerization and photodimerization) in actuating materials such as carbon-based composites[131], hydrogels[132], liquid-crystal polymers[133], and shape-memory polymers (SMPs)[134]. Among them, most photoactuators are triggered by free-space illumination, which requires a line-of-site low-loss optical path between the light source and the actuator. Thus, the utility of these photoactuators requires direct and constant line-of-site access. Besides, the intensity of free-space light may decrease significantly during long-distance transport, especially for the environment with strong absorption and scattering. Moreover, for the free-space light-driven actuators to execute locomotion or handle objects, the control light generally needs to intentionally follow the motion of the actuator. The use of optical fiber can overcome the limitation of the free-space illumination, because light can be transmitted over a long distance with low optical loss through flexible and bendable optical fibers. For example, Zhou et al. introduced a strategy for waveguiding photoactuators based on photothermally addressable nanocomposite hydrogels[135]. Kuenstler et al. demonstrated a photoactuator made of liquid crystal elastomer, achieving reversible bending with a bending angle of 15° and response time of longer than 5 s[40].These reports shed light on the development of waveguide photoactuators, however, all of them suffered from limited bending amplitude and long response time owing to three possible reasons: (1) large thickness of the active layer due to the relatively large size of the commercially available optical fiber (typically >100 μm in diameter); (2) low energy density due to the non-focused light beam; (3) low optical coupling efficiency due to the size mismatch between the optical waveguide and the photoresponsive material.

To address these issues, Xiao et al. employed optical fiber tapers with enhanced optical intensity for high-performance photoactuators with large deformation and fast response[36]. As shown in Fig. 7(a), an optical fiber taper is embedded in a PDMS/Au nanorod (AuNR)-graphene oxide (GO) photothermal film. When a control light is launched into the photothermal film via the fiber taper, photothermal heating induced by the AuNR will cause a significant expansion of the PDMS/AuNR layer due to the high coefficient of thermal expansion (CTE) of PDMS. On the other hand, GO layer undergoes negligible thermal expansion due to its low CTE. Thus, the mismatch between the CTE and deformations of two layers leads to a dramatic bending of the photoactuator. When the light is switched off, the photoactuator recovers back to its initiate state. Benefiting from the special geometric features of fiber taper, i.e., micro/nanoscale diameter and long taper region, the photoactuator features a thin active layer, high energy density and optical coupling efficiency, which enable a fast response of 1.8 s (Fig. 7(b)) and much larger bending angle of 270° (Fig. 7(c)) than that of waveguide actuators reported before. Table 1 provides a performance comparison of the MNF actuator with other types of photoactuators. Owing to its large deformation, the one-arm MNF actuator can grasp an ant (~20 mg) stayed on a tip immediately with the switch on of control laser and then take it off from the tip (Fig. 7(d-i)). The two-arm MNF actuator can capture and lift a group of small balls with a maximum weight of 27 mg (Fig. 7(d-ii)). In addition, the grasped object can be moved with high stability, which is particularly valuable or accurate control when executing a task that requires dynamic location. For example, the two-arm MNF

Table 1 | Comparison of MNF actuators with other types of photoactuators.

Structure	Size (mm)	Bending angle (°)	Response time (s)	Light power (mW)	Ref.
500 μm polymer optical fiber+LCE	~20×0.8	>14	>5	230	ref.[40]
125 μm SMF+LCE	~0.27×0.08	>20	<0.6	10	ref.[41]
MMF+fiber	~20×0.45	>140	>150	800	ref.[42]
80 μm tapered POF+nanocomposite hydrogel	1×0.8×0.3	>60	0.3-0.9	278	ref.[135]
700 nm fiber taper+ GO/AuNR+PDMS	~10×0.5×0.22	>270	<1.8	150	ref.[36]

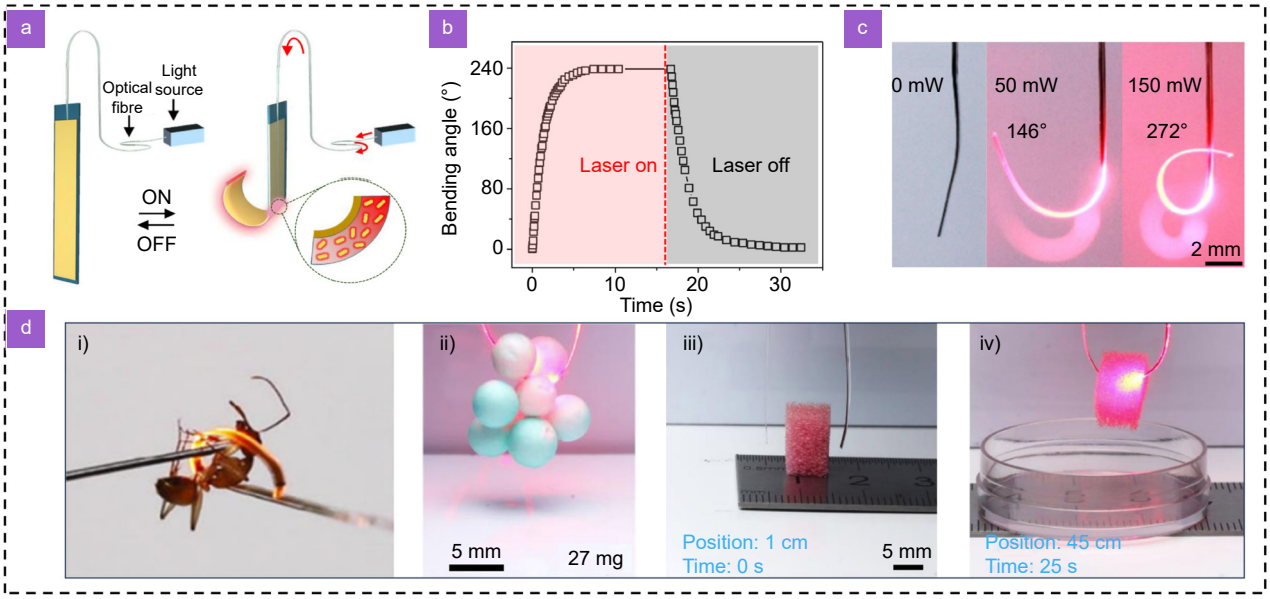

Fig. 7 | MNF enabled photoactuators. (**a**) Schematic of the structure and driving mechanism of the photoactuator. (**b**) Response time of the photoactuator. (**c**) Photographs showing the light-driven bending of a photoactuator under different laser powers. (**d**) One-arm and two-arm OPA gripper capture and move ant (i), glued balls (ii), cuboid (iii, and iv). Figures reproduced with permission from ref.[36], under a Creative Commons Attribution 4.0 International License.

actuator can pick up, transfer, and release a cuboid into a container ~44 cm away from the original place within 25 s (Fig. 7(d-iii, iv)). These results demonstrate the advantages of the MNF actuator in accurately handling objects in a wide operating area, while free-space light-driven actuators suffering from the difficulties in accurately controlling the illuminating spot to follow the moving of actuators during operation.

Outlook

In summary, the recent advances in MNF enabled tactile sensors and photoactuators were reviewed. Looking ahead, we believe that the following issues that may be worth further investigation. Firstly, scalable fabrication of MNF enabled tactile sensors with same performance remains a grant challenge. Although the fabrication of the MNFs can be well controlled, it is still difficult to automatically package MNFs to form uniform tactile sensors. With the rapid development of advanced manufacturing, we believe this issue can be overcome using programable taper drawing machine with the help of highly efficient and dexterous micromanipulation instrument. The reported MNF sensors have shown excellent flexibility, stretchability, and robustness, because the tensile strength of the tiny MNF is typically higher than 5.5 GPa[49]. We found that a well packaged MNF sensor could survive after multiple cycles of a destructive loading of 14.15 MPa, which is almost 140 times atmospheric pressure[129]. On the other hand, light-emitting diode and photodiode can be used as the light source and detector of the MNF sensor, which can dramatically reduce the cost of the sensing system, making it practical in wearable and portable applications. Secondly, human skin is a large area tactile organ with high spatial resolution. Meanwhile, the MNF enabled tactile sensors can only detect the stimuli at one or a few positions. How to realize distributed sensing along the MNF should be a promising field. Thirdly, for soft actuators, how to realize complex deformation and achieve more potential applications, such as searching in unstructured environment, deep-water sampling, and in vivo diagnosis/therapy, need special designs of the actuators and implementation of advanced materials. We believe that the integration of MNF photoactuator and MNF tactile sensor can dramatically enhance the actuator's capability by a closed-loop control. Finally, to meet the increasing demand for novel applications in healthcare, robotics, and metaverse, novel sensing mechanisms or actuating strategies should be introduced into tactile sensors or soft actuators. For example, the fusion of AI algorithm with the flexible opto-electronic devices has significantly improved the sensing ability and haptic feedback experience. In terms of MNF sensors, with the assistance of AI algorithm, one can obtain complex guided modes

evolution information along the tapered region with inhomogeneous diameter accommodating more higher-order modes, which can provide more sensing information. It is possible to achieve an unprecedented spatial resolution for a tapered optical fiber enabled distributed sensor with the help of advanced deep learning technology. When the above-mentioned issues are well addressed, the gap between the lab work and the application of the MNF devices can be significantly mitigated and the MNF sensors or self-sensing MNF photoactuators might be used for biopsy, measuring cell stiffness, manipulating small model organisms (e.g., elegans, larval zebrafish), or detecting pico- to femtonewton force (e.g., radiation pressure), which are difficult to realize with conventional optical sensors or photoactuators.

References

1. Kireev D, Sel K, Ibrahim B et al. Continuous cuffless monitoring of arterial blood pressure via graphene bioimpedance tattoos. *Nat Nanotechnol* **17**, 864–870 (2022).
2. Libanori A, Chen GR, Zhao X et al. Smart textiles for personalized healthcare. *Nat Electron* **5**, 142–156 (2022).
3. Wang G, Badal A, Jia X et al. Development of metaverse for intelligent healthcare. *Nat Mach Intell* **4**, 922–929 (2022).
4. Liu YM, Yiu C, Song Z et al. Electronic skin as wireless human-machine interfaces for robotic VR. *Sci Adv* **8**, eabl6700 (2022).
5. Zhang ZX, Wen F, Sun ZD et al. Artificial intelligence‐enabled sensing technologies in the 5G/internet of things era: from virtual reality/augmented reality to the digital twin. *Adv Intell Syst* **4**, 2100228 (2022).
6. Li GH, Sun FQ, Zhao SK et al. Autonomous electroluminescent textile for visual interaction and environmental warning. *Nano Lett* **23**, 8436–8444 (2023).
7. Shih B, Shah D, Li JX et al. Electronic skins and machine learning for intelligent soft robots. *Sci Robot* **5**, eaaz9239 (2020).
8. Li S, Chen XL, Li XM et al. Bioinspired robot skin with mechanically gated electron channels for sliding tactile perception. *Sci Adv* **8**, eade0720 (2022).
9. Bao RR, Tao J, Zhao J et al. Integrated intelligent tactile system for a humanoid robot. *Sci Bull* **68**, 1027–1037 (2023).
10. Zhou JY, Shao Q, Tang C et al. Conformable and compact multiaxis tactile sensor for human and robotic grasping via anisotropic waveguides. *Adv Mater Technol* **7**, 2200595 (2022).
11. Hou B, Yi LY, Li C et al. An interactive mouthguard based on mechanoluminescence-powered optical fibre sensors for bite-controlled device operation. *Nat Electron* **5**, 682–693 (2022).
12. Leal-Junior A, Avellar L, Biazi V et al. Multifunctional flexible optical waveguide sensor: on the bioinspiration for ultrasensitive sensors development. *Opto-Electron Adv* **5**, 210098 (2022).
13. Bai HD, Li S, Barreiros J et al. Stretchable distributed fiber-optic sensors. *Science* **370**, 848–852 (2020).
14. Zhao HC, O'Brien K, Li S et al. Optoelectronically innervated soft prosthetic hand via stretchable optical waveguides. *Sci Robot* **1**, eaai7529 (2016).
15. Li TL, Su YF, Zheng H et al. An artificial intelligence-motivated skin-like optical fiber tactile sensor. *Adv Intell Syst* **5**, 2200460 (2023).
16. Wang SM, Ni XL, Li LY et al. Noninvasive monitoring of vital signs based on highly sensitive fiber optic mattress. *IEEE Sens J* **20**, 6182–6190 (2020).
17. Massari L, Fransvea G, D'Abbraccio J et al. Functional mimicry of Ruffini receptors with fibre Bragg gratings and deep neural networks enables a bio-inspired large-area tactile-sensitive skin. *Nat Mach Intell* **4**, 425–435 (2022).
18. Li LY, Sheng SF, Liu YF et al. Automatic and continuous blood pressure monitoring via an optical-fiber-sensor-assisted smartwatch. *PhotoniX* **4**, 21 (2023).
19. Guo JJ, Niu MX, Yang CX. Highly flexible and stretchable optical strain sensing for human motion detection. *Optica* **4**, 1285–1288 (2017).
20. Harnett CK, Zhao HC, Shepherd RF. Stretchable optical fibers: threads for strain‐sensitive textiles. *Adv Mater Technol* **2**, 1700087 (2017).
21. Guo JJ, Zhou BQ, Yang CX et al. Stretchable and temperature‐sensitive polymer optical fibers for wearable health monitoring. *Adv Funct Mater* **29**, 1902898 (2019).
22. Leber A, Cholst B, Sandt J et al. Stretchable thermoplastic elastomer optical fibers for sensing of extreme deformations. *Adv Funct Mater* **29**, 1802629 (2019).
23. Guo JJ, Liu XY, Jiang N et al. Highly stretchable, strain sensing hydrogel optical fibers. *Adv Mater* **28**, 10244–10249 (2016).
24. Yin MJ, Zhang YX, Yin ZG et al. Micropatterned elastic gold‐nanowire/polyacrylamide composite hydrogels for wearable pressure sensors. *Adv Mater Technol* **3**, 1800051 (2018).
25. Chen T, Qiao XL, Wei PL et al. Tough gel-fibers as strain sensors based on strain–optics conversion induced by anisotropic structural evolution. *Chem Mater* **32**, 9675–9687 (2020).
26. Zhang L, Tang Y, Tong LM. Micro-/nanofiber optics: merging photonics and material science on nanoscale for advanced sensing technology. *iScience* **23**, 100810 (2020).
27. Li Jh, Chen Jh, Xu F. Sensitive and wearable optical microfiber sensor for human health monitoring. *Adv Mater Technol* **3**, 1800296 (2018).
28. Zhang L, Pan J, Zhang Z et al. Ultrasensitive skin-like wearable optical sensors based on glass micro/nanofibers. *Opto-Electron Adv* **3**, 190022 (2020).
29. Tong LM. Micro/nanofibre optical sensors: challenges and prospects. *Sensors* **18**, 903 (2018).
30. Chen JH, Li DR, Xu F. Optical microfiber sensors: sensing mechanisms, and recent advances. *J Light Technol* **37**, 2577–2589 (2019).
31. Guan BO, Huang YY. Interface sensitized optical microfiber biosensors. *J Light Technol* **37**, 2616–2622 (2019).
32. Li YP, Xu ZL, Tan SJ et al. Recent advances in microfiber sensors for highly sensitive biochemical detection. *J Phys D Appl Phys* **52**, 493002 (2019).
33. Xu YX, Fang W, Tong LM. Real-time control of micro/nanofiber waist diameter with ultrahigh accuracy and precision. *Opt Express* **25**, 10434–10440 (2017).
34. Kang Y, Gong J, Xu YX et al. Ultrahigh-precision diameter

control of nanofiber using direct mode cutoff feedback. *IEEE Photonics Technol Lett* **32**, 219–222 (2020).
35. Yao N, Linghu SY, Xu YX et al. Ultra-long subwavelength micro/nanofibers with low loss. *IEEE Photonics Technol Lett* **32**, 1069–1072 (2020).
36. Xiao JL, Zhou T, Yao N et al. Optical fibre taper-enabled waveguide photoactuators. *Nat Commun* **13**, 363 (2022).
37. Pilz da Cunha M, Debije MG, Schenning APHJ. Bioinspired light-driven soft robots based on liquid crystal polymers. *Chem Soc Rev* **49**, 6568–6578 (2020).
38. El-Atab N, Mishra RB, Al-Modaf F et al. Soft actuators for soft robotic applications: a review. *Adv Intell Syst* **2**, 2000128 (2020).
39. Li JJ, Zhou X, Liu ZF. Recent advances in photoactuators and their applications in intelligent bionic movements. *Adv Opt Mater* **8**, 2000886 (2020).
40. Kuenstler AS, Kim H, Hayward RC. Liquid crystal elastomer waveguide actuators. *Adv Mater* **31**, 1901216 (2019).
41. Zmyślony M, Dradrach K, Haberko J et al. Optical pliers: micrometer-scale, light-driven tools grown on optical fibers. *Adv Mater* **32**, 2002779 (2020).
42. He YC, Liang HH, Chen MH et al. Optical fiber waveguiding soft photoactuators exhibiting giant reversible shape change. *Adv Opt Mater* **9**, 2101132 (2021).
43. Guo JJ, Yang CX, Dai QH et al. Soft and stretchable polymeric optical waveguide-based sensors for wearable and biomedical applications. *Sensors* **19**, 3771 (2019).
44. Wang XC, Li ZL, Su L. Soft optical waveguides for biomedical applications, wearable devices, and soft robotics: a review. *Adv Intell Syst* **6**, 2300482 (2024).
45. Chen MX, Wang Z, Li KW et al. Elastic and stretchable functional fibers: a review of materials, fabrication methods, and applications. *Adv Fiber Mater* **3**, 1–13 (2021).
46. Liu HH, Hu DJJ, Sun QZ et al. Specialty optical fibers for advanced sensing applications. *Opto-Electron Sci* **2**, 220025 (2023).
47. Yang MJ, Yuan ZK, Liu J et al. Photoresponsive actuators built from carbon-based soft materials. *Adv Opt Mater* **7**, 1900069 (2019).
48. Costil R, Holzheimer M, Crespi S et al. Directing coupled motion with light: a key step toward machine-like function. *Chem Rev* **121**, 13213–13237 (2021).
49. Tong LM, Gattass RR, Ashcom JB et al. Subwavelength-diameter silica wires for low-loss optical wave guiding. *Nature* **426**, 816–819 (2003).
50. Wu XQ, Tong LM. Optical microfibers and nanofibers. *Nanophotonics* **2**, 407–428 (2013).
51. Zhang L, Gu FX, Lou JY et al. Fast detection of humidity with a subwavelength-diameter fiber taper coated with gelatin film. *Opt Express* **16**, 13349–13353 (2008).
52. Fang HB, Xie Y, Yuan ZP et al. Parallel fabrication of silica optical microfibers and nanofibers. *Light Adv Manuf* **5**, 20 (2024).
53. Liu N, Yao N, Wang SP et al. An optical nanofibre-enabled on-chip single-nanoparticle sensor. *Lab Chip* **23**, 4901–4908 (2023).
54. Pan J, Zhang Z, Jiang CP et al. A multifunctional skin-like wearable optical sensor based on an optical micro-/nanofibre. *Nanoscale* **12**, 17538–17544 (2020).
55. Lou JY, Tong LM, Ye ZZ. Modeling of silica nanowires for optical sensing. *Opt Express* **13**, 2135–2140 (2005).
56. Luo W, Chen Y, Xu F. Recent progress in microfiber-optic sensors. *Photonic Sens* **11**, 45–68 (2021).
57. Sun LP, Huang YY, Guan BO. Microfiber interferometric biosensors. *Laser Optoelectron Prog* **58**, 1306004 (2021).
58. Tong LM. Recent progress in optical micro/nanofiber technology. *Acta Opt Sin* **42**, 1706001 (2022).
59. Sumetsky M, Dulashko Y, Fini JM et al. Optical microfiber loop resonator. *Appl Phys Lett* **86**, 161108 (2005).
60. Jiang XS, Song QH, Xu L et al. Microfiber knot dye laser based on the evanescent-wave-coupled gain. *Appl Phys Lett* **90**, 233501 (2007).
61. White IM, Oveys H, Fan XD. Liquid-core optical ring-resonator sensors. *Opt Lett* **31**, 1319–1321 (2006).
62. Wang SS, Hu ZF, Li YH et al. All-fiber Fabry-Perot resonators based on microfiber Sagnac loop mirrors. *Opt Lett* **34**, 253–255 (2009).
63. Kou JL, Feng J, Wang QJ et al. Microfiber-probe-based ultrasmall interferometric sensor. *Opt Lett* **35**, 2308–2310 (2010).
64. Jiang BQ, Hou YG, Wu JX et al. In-fiber photoelectric device based on graphene-coated tilted fiber grating. *Opto-Electron Sci* **2**, 230012 (2023).
65. Zhang Y, Lin B, Tjin SC et al. Refractive index sensing based on higher-order mode reflection of a microfiber Bragg grating. *Opt Express* **18**, 26345–26350 (2010).
66. Liu YX, Meng C, Zhang AP et al. Compact microfiber Bragg gratings with high-index contrast. *Opt Lett* **36**, 3115–3117 (2011).
67. Sun LP, Li J, Jin L et al. Structural microfiber long-period gratings. *Opt Express* **20**, 18079–18084 (2012).
68. Li BL, Chen JH, Xu F et al. Periodic micro-structures in optical microfibers induced by Plateau-Rayleigh instability and its applications. *Opt Express* **25**, 4326–4334 (2017).
69. Xuan HF, Jin W, Zhang M. CO_2 laser induced long period gratings in optical microfibers. *Opt Express* **17**, 21882–21890 (2009).
70. Li YH, Tong LM. Mach-Zehnder interferometers assembled with optical microfibers or nanofibers. *Opt Lett* **33**, 303–305 (2008).
71. Zheng YZ, Dong XY, Chan CC et al. Optical fiber magnetic field sensor based on magnetic fluid and microfiber mode interferometer. *Opt Commun* **336**, 5–8 (2015).
72. Luo YF, Abidian MR, Ahn JH et al. Technology roadmap for flexible sensors. *ACS Nano* **17**, 5211–5295 (2023).
73. Li W, Hu ZF, Li XY et al. High-sensitivity microfiber strain and force sensors. *Opt Commun* **314**, 28–30 (2014).
74. Yu XC, Zhi YY, Tang SJ et al. Optically sizing single atmospheric particulates with a 10-nm resolution using a strong evanescent field. *Light Sci Appl* **7**, 18003 (2018).
75. Mei HY, Pan J, Zhang Z et al. Coiled optical nanofiber for optofluidic absorbance detection. *ACS Sens* **4**, 2267–2271 (2019).
76. Cai DW, Tong T, Zhang Z et al. Functional film coated optical micro/nanofibers for high-performance gas sensing. *IEEE Sens J* **19**, 9229–9234 (2019).
77. Jiang XS, Tong LM, Vienne G et al. Demonstration of optical microfiber knot resonators. *Appl Phys Lett* **88**, 223501 (2006).
78. Sumetsky M, Dulashko Y, Fini JM et al. The microfiber loop resonator: theory, experiment, and application. *J Light Technol* **24**, 242–250 (2006).
79. Vienne G, Li YH, Tong LM. Effect of host polymer on

microfiber resonator. *IEEE Photonics Technol Lett* **19**, 1386–1388 (2007).
80. Xu F, Brambilla G. Embedding optical microfiber coil resonators in Teflon. *Opt Lett* **32**, 2164–2166 (2007).
81. Lu JS, Ginis V, Qiu CW et al. Polarization-dependent forces and torques at resonance in a microfiber-microcavity system. *Phys Rev Lett* **130**, 183601 (2023).
82. Zhang YN, Gao J, Xia F et al. Microfiber knot resonators: structure, spectral properties, and sensing applications. *Laser Photonics Rev* **18**, 2300765 (2024).
83. Xu ZL, Luo YY, Sun QZ et al. Light velocity control in monolithic microfiber bridged ring resonator. *Optica* **4**, 945–950 (2017).
84. Chen Y, Yan SC, Zheng X et al. A miniature reflective microforce sensor based on a microfiber coupler. *Opt Express* **22**, 2443–2450 (2014).
85. Luo HP, Sun QZ, Xu ZL et al. Microfiber-based inline mach–zehnder interferometer for dual-parameter measurement. *IEEE Photonics J* **7**, 7100908 (2015).
86. Wang PF, Ding M, Bo L et al. Fiber-tip high-temperature sensor based on multimode interference. *Opt Lett* **38**, 4617–4620 (2013).
87. Li YP, Tan SJ, Yang LY et al. Optical microfiber neuron for finger motion perception. *Adv Fiber Mater* **4**, 226–234 (2022).
88. Li KW, Zhang T, Liu GG et al. Ultrasensitive optical microfiber coupler based sensors operating near the turning point of effective group index difference. *Appl Phys Lett* **109**, 101101 (2016).
89. Yan SC, Liu ZY, Li C et al. "Hot-wire" microfluidic flowmeter based on a microfiber coupler. *Opt Lett* **41**, 5680–5683 (2016).
90. Zhang Z, Yao N, Pan J et al. A new route for fabricating polymer optical microcavities. *Nanoscale* **11**, 5203–5208 (2019).
91. Wang X, Zhou HY, Chen MH et al. Highly sensitive strain sensor based on microfiber coupler for wearable photonics healthcare. *Adv Intell Syst* **5**, 2200344 (2023).
92. Song XD, Wang Q, Liu QL et al. Twisted optical micro/nanofibers enabled detection of subtle temperature variation. *ACS Appl Mater Interfaces* **15**, 47177–47183 (2023).
93. Yu W, Yao N, Pan J et al. Highly sensitive and fast response strain sensor based on evanescently coupled micro/nanofibers. *Opto-Electron Adv* **5**, 210101 (2022).
94. Ran Y, Tan YN, Sun LP et al. 193 nm excimer laser inscribed Bragg gratings in microfibers for refractive index sensing. *Opt Express* **19**, 18577–18583 (2011).
95. Kou JL, Ding M, Feng J et al. Microfiber-based Bragg gratings for sensing applications: a review. *Sensors* **12**, 8861–8876 (2012).
96. Yue X, Lu RY, Yang QC et al. Flexible wearable optical sensor based on optical microfiber bragg grating. *J Light Technol* **41**, 1858–1864 (2023).
97. Meng KY, Xiao X, Wei WX et al. Wearable pressure sensors for pulse wave monitoring. *Adv Mater* **34**, 2109357 (2022).
98. Wang S, Xiao JL, Liu HT et al. Silk nanofibrous iontronic sensors for accurate blood pressure monitoring. *Chem Eng J* **453**, 139815 (2023).
99. Lin QP, Huang J, Yang JL et al. Highly sensitive flexible iontronic pressure sensor for fingertip pulse monitoring. *Adv Healthc Mater* **9**, 2001023 (2020).
100. Li LY, Liu YF, Song CY et al. Wearable alignment-free microfiber-based sensor chip for precise vital signs monitoring and cardiovascular assessment. *Adv Fiber Mater* **4**, 475–486 (2022).
101. Park J, Kim M, Lee Y et al. Fingertip skin-inspired microstructured ferroelectric skins discriminate static/dynamic pressure and temperature stimuli. *Sci Adv* **1**, e1500661 (2015).
102. Yao N, Wang XY, Ma SQ et al. Single optical microfiber enabled tactile sensor for simultaneous temperature and pressure measurement. *Photonics Res* **10**, 2040–2046 (2022).
103. Zhu HT, Zhan LW, Dai Q et al. Self-assembled wavy optical microfiber for stretchable wearable sensor. *Adv Opt Mater* **9**, 2002206 (2021).
104. Zhu HT, Luo JX, Dai Q et al. Spatiotemporal hemodynamic monitoring via configurable skin-like microfiber Bragg grating group. *Opto-Electron Adv* **6**, 230018 (2023).
105. Zhang Z, Kang YR, Yao N et al. A multifunctional airflow sensor enabled by optical micro/nanofiber. *Adv Fiber Mater* **3**, 359–367 (2021).
106. Mishra P, Kumar H, Sahu S et al. Flexible and wearable optical system based on u-shaped cascaded microfiber interferometer. *Adv Mater Technol* **8**, 2200661 (2023).
107. Yang LY, Li YP, Fang F et al. Highly sensitive and miniature microfiber-based ultrasound sensor for photoacoustic tomography. *Opto-Electron Adv* **5**, 200076 (2022).
108. Ma J, Zhao J, Chen HW et al. Transparent microfiber Fabry-Perot ultrasound sensor with needle-shaped focus for multiscale photoacoustic imaging. *Photoacoustics* **30**, 100482 (2023).
109. Shum PP, Keiser G, Humbert G et al. Highly sensitive microfiber ultrasound sensor for photoacoustic imaging. *Opto-Electron Adv* **6**, 230065 (2023).
110. Ko SH, Rogers J. Functional materials and devices for XR (VR/AR/MR) applications. *Adv Funct Mater* **31**, 2106546 (2021).
111. Kim H, Kwon YT, Lim HR et al. Recent advances in wearable sensors and integrated functional devices for virtual and augmented reality applications. *Adv Funct Mater* **31**, 2170289 (2021).
112. Zhu ML, Sun ZD, Lee C. Soft modular glove with multimodal sensing and augmented haptic feedback enabled by materials' multifunctionalities. *ACS Nano* **16**, 14097–14110 (2022).
113. Li Y, Yang LN, He ZM et al. Low-cost data glove based on deep-learning-enhanced flexible multiwalled carbon nanotube sensors for real-time gesture recognition. *Adv Intell Syst* **4**, 2200128 (2022).
114. Zhao YL, Liu JL, Lian C et al. A single smart ring for monitoring 20 kinds of multi-intensity daily activities-from kitchen work to fierce exercises. *Adv Intell Syst* **4**, 2270058 (2022).
115. Tan PC, Han X, Zou Y et al. Self-powered gesture recognition wristband enabled by machine learning for full keyboard and multicommand input. *Adv Mater* **34**, 2200793 (2022).
116. Fang H, Wang L, Fu ZZ et al. Anatomically designed triboelectric wristbands with adaptive accelerated learning for human-machine interfaces. *Adv Sci* **10**, 2205960 (2023).
117. Luo YY, Li YZ, Sharma P et al. Learning human-environment interactions using conformal tactile textiles. *Nat Electron* **4**, 193–201 (2021).
118. Araromi OA, Graule MA, Dorsey KL et al. Ultra-sensitive and resilient compliant strain gauges for soft machines. *Nature* **587**, 219–224 (2020).
119. Yang J, Zhou J, Tao GM et al. Wearable 3.0: from smart clothing to wearable affective robot. *IEEE Netw* **33**, 8–14 (2019).

120. Wang SP, Wang XY, Wang S et al. Optical-nanofiber-enabled gesture-recognition wristband for human-machine interaction with the assistance of machine learning. *Adv Intell Syst* **5**, 2200412 (2023).
121. Weng W, Yang JJ, Zhang Y et al. A route toward smart system integration: from fiber design to device construction. *Adv Mater* **32**, 1902301 (2020).
122. Ma SQ, Wang XY, Li P et al. Optical micro/nano fibers enabled smart textiles for human-machine interface. *Adv Fiber Mater* **4**, 1108–1117 (2022).
123. Li T, Li LH, Sun HW et al. Porous ionic membrane based flexible humidity sensor and its multifunctional applications. *Adv Sci* **4**, 1600404 (2017).
124. Zhou KK, Xu WJH, Yu YF et al. Tunable and nacre-mimetic multifunctional electronic skins for highly stretchable contact-noncontact sensing. *Small* **17**, 2100542 (2021).
125. Liu HT, Song XD, Wang XY et al. Optical microfibers for sensing proximity and contact in human-machine interfaces. *ACS Appl Mater Interfaces* **14**, 14447–14454 (2022).
126. Li GZ, Liu SQ, Wang LQ et al. Skin-inspired quadruple tactile sensors integrated on a robot hand enable object recognition. *Sci Robot* **5**, eabc8134 (2020).
127. Kim T, Kim J, You I et al. Dynamic tactility by position-encoded spike spectrum. *Sci Robot* **7**, eabl5761 (2022).
128. Jiang CP, Zhang Z, Pan J et al. Finger-skin-inspired flexible optical sensor for force sensing and slip detection in robotic grasping. *Adv Mater Technol* **6**, 2100285 (2021).
129. Tang Y, Yu LT, Pan J et al. Optical nanofiber skins for multifunctional humanoid tactility. *Adv Intell Syst* **5**, 2200203 (2023).
130. Tang Y, Liu HT, Pan J et al. Optical micro/nanofiber-enabled compact tactile sensor for hardness discrimination. *ACS Appl Mater Interfaces* **13**, 4560–4566 (2021).
131. Han B, Zhang YL, Chen QD et al. Carbon-based photothermal actuators. *Adv Funct Mater* **28**, 1802235 (2018).
132. Jiao DJ, Zhu QL, Li CY et al. Programmable morphing hydrogels for soft actuators and robots: from structure designs to active functions. *Acc Chem Res* **55**, 1533–1545 (2022).
133. Liu C, Ji SB, Xu HP. Rapidly reprogrammable actuation of liquid crystal elastomers. *Matter* **5**, 2409–2413 (2022).
134. Peng WJ, Zhang GG, Liu J et al. Light-coded digital crystallinity patterns toward bioinspired 4D transformation of shape-memory polymers. *Adv Funct Mater* **30**, 2000522 (2020).
135. Zhou Y, Hauser AW, Bende NP et al. Waveguiding microactuators based on a photothermally responsive nanocomposite hydrogel. *Adv Funct Mater* **26**, 5447–5452 (2016).

Acknowledgements

We are grateful for financial supports from the National Natural Science Foundation of China (No. 61975173), the Key Research and Development Project of Zhejiang Province (No. 2022C03103, 2023C01045).

Competing interests

The authors declare no competing financial interests.

Scan for Article PDF